An empirically derived emission algorithm for wind-blown dust

Roland R. Draxler,[1] Paul Ginoux,[2] and Ariel F. Stein[1,3]

Received 8 September 2009; revised 26 January 2010; accepted 2 April 2010; published 31 August 2010.

[1] A wind-blown dust emission algorithm was developed by matching the frequency of high–aerosol optical depth (AOD) events derived from the MODIS Deep Blue algorithm with the frequency of friction velocities derived from National Centers for Environmental Prediction's North American Mesoscale model. The threshold friction velocity is defined as the velocity that has the same frequency of as the 0.75 AOD. The AODs are converted to an emission flux that is used to compute the linear regression slope of the flux to the friction velocity. The slope represents the potential of a particular land surface to produce airborne dust and, in combination with the friction velocity, is used as a predictor for wind-blown dust emissions. Calculations for a test period of June and July 2007 showed the model prediction to capture the major measured plume events in timing and magnitude, although peak events tended to be overpredicted and many of the near-background level ambient concentrations were underpredicted. Most of the airborne dust loadings are attributed to locations with relatively low threshold friction velocities (<45 cm s^{-1}), although these locations only composed of 9% of the total number of source locations. There was some evidence that the duration of wind-blown dust plume events was comparable to the 3 day sampling frequency of the IMPROVE monitoring network. Higher temporal frequency AIRNow observations at Phoenix showed a surprisingly good fit with the magnitude of the model-predicted peak concentrations.

Citation: Draxler, R. R., P. Ginoux, and A. F. Stein (2010), An empirically derived emission algorithm for wind-blown dust, *J. Geophys. Res.*, *115*, D16212, doi:10.1029/2009JD013167.

1. Introduction

[2] The results of an initial investigation to develop a wind-blown dust emissions module for North America that can eventually be incorporated into the National Oceanic and Atmospheric Administration's (NOAA) emerging air quality forecast capability [*Davidson et al.*, 2008] are described in the following sections. The requirements for such a capability are focused on short transport distances and time scales. Furthermore, the absence of large dust-producing regions in North America, common in Asia and Africa, elevates the importance of correctly identifying the spatial distribution of dust sources.

[3] The mechanism for wind-blown dust emission is assumed to be a combination of mechanical forces such as "sand-blasting" and "self-abrasion" with the wind-driven surface stress providing aerodynamic lift to the soil particles. The larger particles that cannot become airborne bounce along the surface (saltation) causing additional smaller particles to become airborne. The net vertical flux of emitted material can then be dispersed and transported. A number of entrainment mechanisms of varying complexity have been developed [*Iversen and White*, 1982; *Shao et al.*, 1993; *Marticorena and Bergametti*, 1995], and these mechanisms have been applied with some variations to a number of different modeling systems [*Nickovic et al.*, 2001; *Perez et al.*, 2006; *Liu and Westphal*, 2001; *Ginoux et al.*, 2001; *Morcrette et al.*, 2008; *Uno et al.*, 2006]. *Darmenova et al.* [2009] provide a review and comparison of two of the most complex, physically based schemes based upon surface characteristics that partition the fluxes into a horizontal component representing the drifting sand and vertical component which results in airborne transport. Regardless of the approach, all methods require the determination of several spatially and temporally varying parameters that describe the soil morphology and the interaction of the meteorological environment with the surface.

[4] For instance, a module for the emission of mineral dust particulate matter with diameters of less that 10 μm (PM_{10}) had initially been developed [*Gillette et al.*, 1997] using the concept of a spatially dependent threshold friction velocity based upon the work of *Marticorena et al.* [1997]. The dust emission flux [$Ku_*(u_*^2 - u_{*t}^2)$] is computed for each location where the friction velocity (u_*) exceeds a predefined threshold friction velocity (u_{*t}) based upon the soil characteristics (K) at each location. For instance, *Draxler et al.* [2001] tested the emission algorithm in conjunction with the HYSPLIT (Hybrid Single-Particle Lagrangian Integrated Trajectory) [*Draxler and Hess*, 1998] model over Kuwait, Iraq, and Saudi Arabia. The model simulates pol-

[1]Air Resources Laboratory, NOAA, Silver Spring, Maryland, USA.
[2]Geophysical Fluid Dynamics Laboratory, NOAA, Princeton, New Jersey, USA.
[3]Earth Resources Technology, Silver Spring, Maryland, USA.

Copyright 2010 by the American Geophysical Union.
0148-0227/10/2009JD013167

lutant transport and dispersion by following the motion of individual particles in a wind field and dispersing them with a random motion component proportional to the atmospheric turbulence. For these simulations, the model predicted about the right number of dust events and agreed quantitatively with measurements at four locations in Saudi Arabia and one in Kuwait. However, for several smaller-scale dust events, the model substantially overpredicted the air concentrations. Part of the overprediction was attributed to the model's sensitivity to u_{*t} and K and the difficulty in accurately representing these parameters in the model.

[5] For application to other domains where detailed digital soil characteristics are not always available, the emission module was modified to use a simpler formulation (dust emission flux = $0.01u_*^4$), which was first proposed by *Westphal et al.* [1987] and is not dependent upon the soil characteristics. In this variation of the emission module, potential dust-producing areas were defined by assuming that emissions could occur from any land use grid cell defined as a desert. The lower emission flux of the Westphal's equation, compared to the Gillette approach, was compensated by the greater number of potential dust emission cells defined by using a broad desert definition for all the dust producing regions. This model variation was tested by *Escudero et al.* [2006] for dust emissions from North Africa, and the results compared quite favorably with high daily ambient PM_{10} levels recorded at three Spanish EMEP (Cooperative Program for Monitoring and Evaluation of the Long-Range Transmission of Air Pollutants in Europe) regional background monitoring stations, located over the central Iberian Peninsula, during a North African dust outbreak from 12 to 15 March 2003.

[6] An investigation into the suitability of applying the revised dust emission module over North America quickly showed that the airborne dust loadings were substantially overpredicted using either of the two previous simplified emission schemes, because neither the soil coefficients nor threshold friction velocities were representative of the continental United States. This is not entirely unexpected as the previous approach was linked with "active desert sand sheets," which are not present in North America to the same extent as in other parts of the world. Redefining the dust emission regions to correspond with geographic depressions where silt deposits have accumulated [*Ginoux et al.*, 2001] was not sufficient for this application either as the two critical parameters (u_{*t} and K) are still unresolved.

[7] In order to determine the wind-blown dust emission factors, an empirically derived approach using the MODIS (Moderate Resolution Imaging Spectroradiometer) AOD (Aerosol Optical Depth) values is developed in this analysis. After several preprocessing steps to remove nonmineral dust sources, *Ginoux et al.* [2010] presented a 4 year climatology of the MODIS AODs computed using the Deep Blue algorithm and represented as the "frequency of occurrence" (FOO) for seven levels of AOD (0.25, 0.5, 0.75, 1, 1.5, 2, and 3). They attributed AOD values at 0.75 and higher primarily to natural sources. We use those AOD statistical results in combination with independently determined statistics of friction velocity at the same grid points to compute the dust emission required to reproduce the AOD values. The end result of this analysis is a "simple" dust emission algorithm where, unlike other simple methods, the emission factors and threshold velocities vary in both space and time.

[8] Ideally, the development of a dust emission algorithm should use friction velocities computed at the same time and location as each MODIS AOD value. However, the high-resolution meteorological data period does not overlap the AOD analysis period, and therefore, a statistical approach was used to determine the emission algorithm constants, where we must assume that the individual periods are representative of a longer-term average. In future dust forecasting applications, the modeling technique needs to work over other time periods than the period over which the model was developed, which is consistent with the use of a statistical approach to determine emissions.

2. Dust Emission Algorithm

[9] In the following sections, we describe how the satellite-derived AOD values are used in conjunction with a meteorological model's computed friction velocity to estimate the dust emissions required to reproduce the AOD values. The end result of this analysis is a dust emission algorithm with emission factors and friction threshold velocities varying in both space and time.

2.1. Aerosol Optical Depth

[10] The retrieval of aerosol properties over land, including deserts, from the MODIS Deep Blue algorithm allows for the direct attribution of dust sources of natural origin. The Deep Blue algorithm employs radiances from the blue channels of satellite instruments, at which wavelengths the surface reflectance is low enough that the presence of dust brightens the total reflectance and enhances the spectral contrast [*Hsu et al.*, 2004]. The Deep Blue algorithm has been applied operationally to the MODIS instrument on the Aqua platform.

[11] A detailed description of the retrieval algorithm is given by *Hsu et al.* [2004], and we present only a brief overview. After screening for clouds, the surface reflectance for a given pixel is determined from a clear-scene georeferenced data base. The reflectance at 412, 470, and 670 nm is compared to precalculated radiances at different viewing angles, surface reflectance, AOD, and ω, the single scattering albedo [*Hsu et al.*, 2006]. A minimization procedure is then applied to determine the mixing ratio between various dust and smoke models that best fits the calculated and observed spectral reflectance. For the mixing ratio that produces the best match, the values of AOD and ω at 412, 550, and 670 nm and the Angstrom parameter (α) are reported. These aerosol products are the only multiyear global daily spectral data available and are used to detect scenes with freshly emitted dust by screening out of aged transported dust and other aerosol components.

[12] Freshly emitted dust is characterized by large particles that have not yet been removed by gravitational settling. *Maring et al.* [2003] have observed that particles greater than 7.3 μm are efficiently removed during transport, but once the largest particles are removed the normalized size distribution does not change over days. The rapid shift of the size distribution from coarse freshly emitted dust toward stable fine-aged dust provides a method to isolate sources from lingering dust. Also, there is a strong contrast between

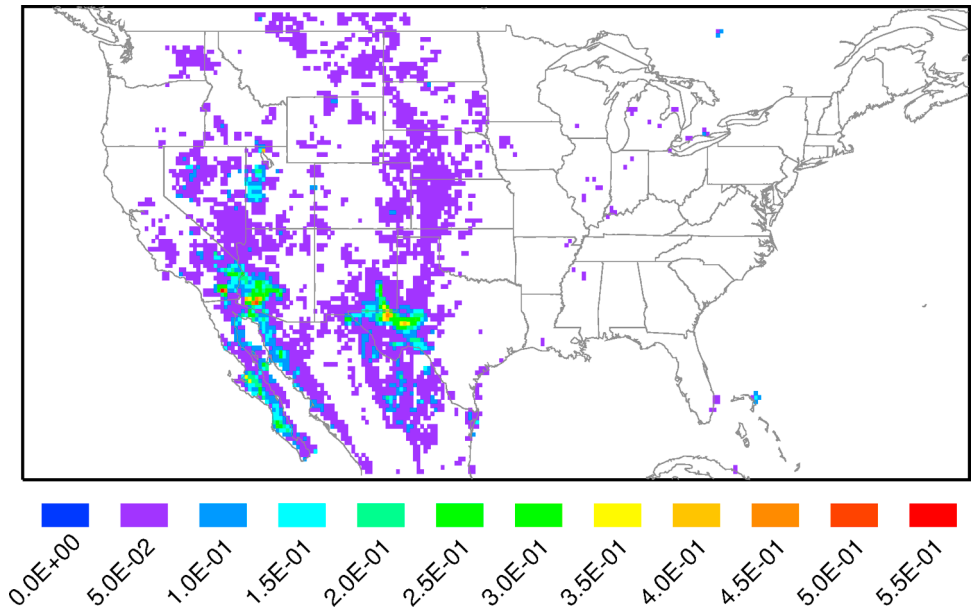

Figure 1. The annually averaged frequency of daily occurrence (FOO) for AOD = 0.75 from the MODIS Deep Blue analysis showing 3524 grid cells with nonzero AOD.

coarse mode dust particles and accumulation mode (radius < 0.5 μm) of biomass burning and urban aerosols. Therefore, a parameter sensitive to the size distribution should allow the separation of not only dust from other aerosol types but also freshly emitted dust from aged dust. *Eck et al.* [1999] have shown that the dominance of one mode over the other can be measured with the Angstrom wavelength exponent (α). The α values range from −0.5 to 1 in dusty environments and higher in polluted regions [*Dubovik et al.*, 2002]. As the largest particles are removed from the atmosphere by gravitational settling, aged dust will contain smaller particles characterized by a higher α value. A low cutoff value of α = 0.0 is prescribed for freshly emitted dust.

[13] A second screening parameter is also applied, and it is based on the spectral dependence of absorption properties of dust. As opposed to smoke aerosols, dust absorption decreases with wavelength from its peak in the near ultraviolet [*Sokolik and Toon*, 1999; *Koven and Fung*, 2006]. The single scattering albedo (ω) is the ratio of the scattering efficiency by the sum of scattering and absorption efficiencies. Its value decreases with increasing absorption. By using the spectral difference of ω at 412 nm (deep blue) and 670 nm (red), scenes with absorption due to dust can be selected. The combination of both screening parameters can be used to detect active dust sources. However, as the contribution of dust to AOD decreases for weak sources compared to other aerosol types, a minimum value of around AOD = 0.75 is suggested by *Ginoux et al.* [2010].

[14] This technique was first demonstrated over Africa [*Ginoux et al.*, 2010] and was applied globally by interpolating the MODIS geolocated level 2 data (10 km pixels) to a 0.1° resolution grid. However, in this study, the level 2 data have been interpolated to a 0.25° grid. Data from January 2003 to December 2006 were processed to keep only scenes with coarse dust particles by using the spectral values of ω and α. The processed AOD data are presented as a frequency of occurrence (FOO). The FOO is calculated by counting the days of one particular month over 4 years with AOD greater than the bin value divided by the total number of days with valid MODIS data (no clouds, Sun glint, or instrumental problems). The sources are identified on a monthly basis using 4 years of data from the persistence of significant aerosol optical depth of freshly emitted dust. The natural or anthropogenic attribution of dust sources was established from a land use data set. For a daily optical depth of 0.75 or higher, *Ginoux et al.* [2010] showed that only natural dust has a significant FOO. Although all of our calculations were done by month, the summary of the emission processing results in the following illustrations show the annual values for each step.

2.2. Threshold Friction Velocity

[15] The threshold friction velocity is determined at each grid cell by equating the FOO of AOD = 0.75 (Figure 1) to the friction velocity at that location with the same FOO. Note that the bulk of the grid points shown in Figure 1 show very low FOO values with a median value of only 0.01. Only four regions show more frequent AOD events, with the two largest regions covering western Texas and the California-Arizona border. The friction velocities with the same FOO as the 0.75 AOD represent the threshold below which no dust emissions are assumed to occur. However, for a grid cell to have sufficient dust emissions to compute an emission rate that can be attributed to natural sources, there also needs to be a nonzero FOO at higher AOD levels. The FOO for AOD = 1.0 is shown in Figure 2, and there is a substantial decrease (3524–1805) in the number of grid cells with nonzero FOO. Note that the number of potential emission cells also varies by month with the spring-summer period (March–July) showing about 3 times as many potential emission points as the autumn-winter period (September–February) presumably due to seasonal variations in soil moisture, land cover, and wind velocity.

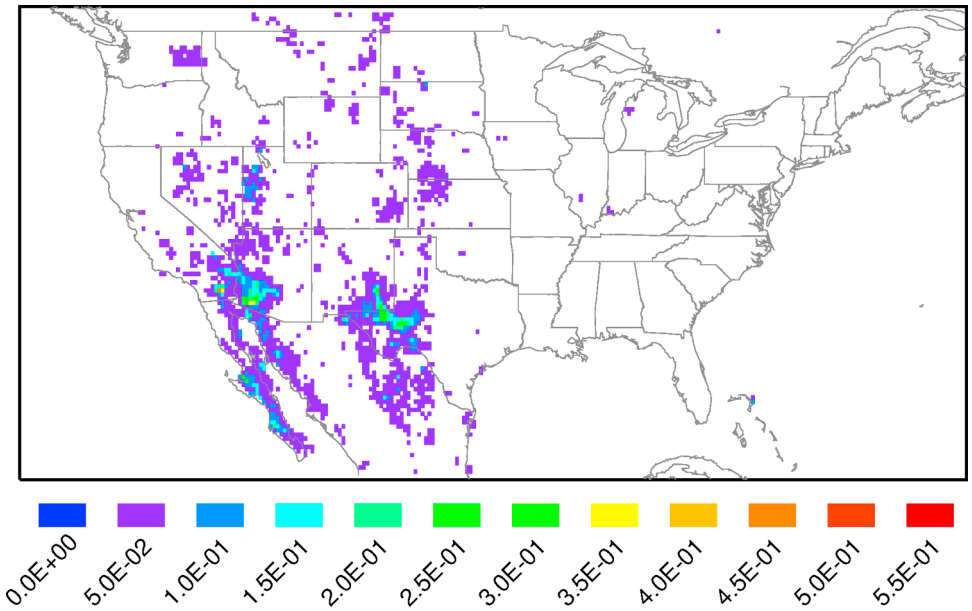

Figure 2. The annual frequency of occurrence (FOO) for AOD = 1.0 from the MODIS Deep Blue analysis showing 1805 grid cells with nonzero AOD.

[16] The friction velocities associated with each grid point in Figure 2 were extracted for each hour from archived fields of NOAA's National Centers for Environmental Prediction (NCEP) 12 km North American Mesoscale (NAM) forecast model [*Janjic*, 2003; *Janjic et al.*, 2001] for May 2008 through April 2009. Prior to January 2008, hourly 12 km resolution NAM data were not archived. Because the NAM is run 4 times per day, the archive consists of a time series of short-term forecasts out to +5 h. The meteorology is evaluated over a time window corresponding to the time of observation by the MODIS instrument on the Aqua platform, about 1330 LST. Considering that most dust-producing grid points are in the western United States (+7 h UTC), the average observation time would correspond to 2100 UTC. Also a few hours prior and just after (1500–2300 UTC) the observation are included to capture all the possible dust events that might contribute to the observation. The monthly time series of friction velocities at each grid point were then sorted, and the threshold friction velocity was assigned to each grid point as the friction velocity with the same FOO as the AOD at the 0.75 level. On average, there is a 5% variation in friction velocity between each AOD bin. The annual average results for the threshold friction velocities are shown in Figure 3. It should be noted

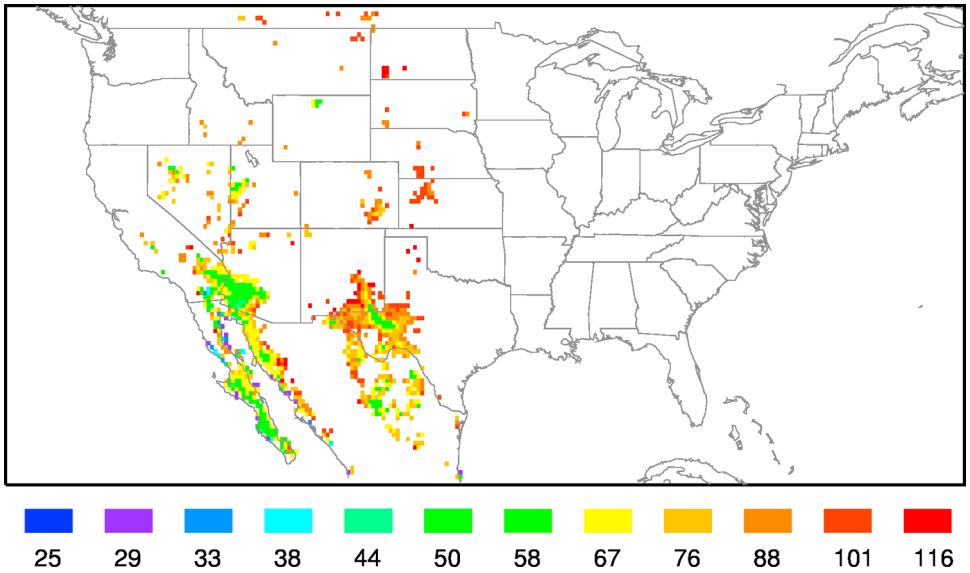

Figure 3. The areal distribution of the annual average threshold friction velocity (cm s^{-1}), which is defined as the friction velocity with the same FOO as the AOD in Figure 1 for grid cells that also have AOD values defined as shown in Figure 2.

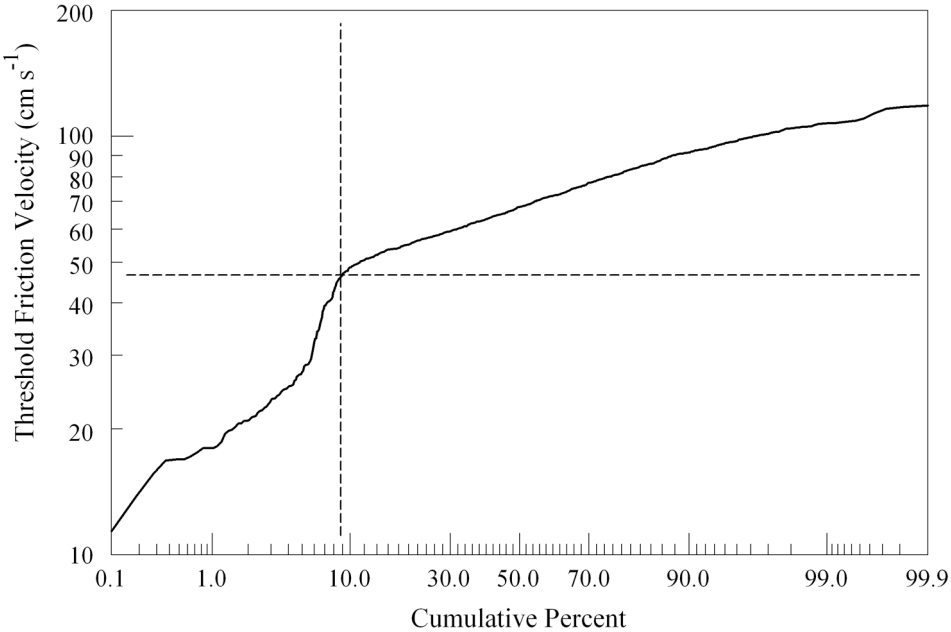

Figure 4. The cumulative frequency distribution of the annual average threshold friction velocities for the locations shown in Figure 2.

that these friction velocities were derived from the boundary layer scheme used by the NCEP model and may not be applicable to friction velocities derived from other models or observations.

[17] In an attempt to determine the representativeness of the computed threshold friction velocities, the cumulative frequency distribution of the annual average velocities that were used to create Figure 3 is computed, and the result is shown in Figure 4. There appears to be two different distributions, with the bulk of the data (91%) showing values above 45 cm s^{-1}. These results are consistent with the two regimes found by *Marticorena et al.* [1997] for disturbed or noncrusted soils (smooth surfaces) and rain or biologically formed crusted soils (rough surfaces), the latter having threshold friction velocities above 50 cm s^{-1}. Although they concluded that the smoother soil surfaces would be the most active wind-blown dust sources in normal conditions, there are 10 times as many more rough surfaces that could contribute to wind-blown dust in this region if the higher threshold friction velocities are exceeded.

2.3. Emission Flux

[18] Converting the AOD values to airborne mass and dividing by the time period that the friction velocity exceeds the threshold results in an emission flux (q). Essentially, we are assuming that the duration of the dust storm event equals the time duration that the friction velocity exceeds the threshold friction velocity. The conversion of AOD to column mass follows *Perez et al.* [2006], where AOD = 0.5 m^2 g^{-1} times the column mass g m^{-2}, which corresponds to a monomodal distribution with a radius of approximately 2 μm. This particular size represents the maximum of the mass size distribution near the emission sources [*D'Almeida*, 1987]. The column mass was also corrected for deposition by adding in the mass lost over the emission period by computing the dust particle's gravitational settling velocity. The correction was minor (<1%) for typical afternoon boundary layer depths (2 km). Each grid point may have up to five AOD values (0.75, 1.0, 1.5, 2.0, and 3.0), and there is a friction velocity associated with each AOD FOO. Although AOD = 0.75 represents our assumed wind-blown dust threshold, this is not an absolute delimiter between natural wind-blown emissions and perhaps other anthropogenic sources or even thin cirrus cloud contamination [*Hsu et al.*, 2004]. At higher AOD values, the natural sources become more dominant [*Ginoux et al.*, 2010]. To minimize the anthropogenic contribution to the emission flux, the column mass for AOD = 0.75 is subtracted from the emission calculation. Although this value represents a rather large aerosol mass, it will have a rapidly diminishing influence on grid points that also have a nonzero FOO for higher AOD values and it greatly reduces the contribution of the majority of grid points that are associated with a very small FOO. Seventy-five percent of the grid points shown in Figure 1 have a FOO of 0.03 or less. At AOD = 0.75, *Ginoux et al.* [2010] found that about half the grid points are associated with anthropogenic emissions, and we are in effect removing the mass contribution from those grid points shown in Figure 1 but not in Figure 2. Although we might be removing some dust sources in this process, this procedure effectively insures that only natural wind-blown dust sources are used in the subsequent calculations.

[19] Following a similar approach as in previous wind-blown dust modeling studies, the emission flux (g m^{-2} s^{-1}),

$$q = Kf(u_*), \tag{1}$$

can be defined as the product of a soil factor and some function of the friction velocity. In those previously cited studies, this functional form may have been related to the

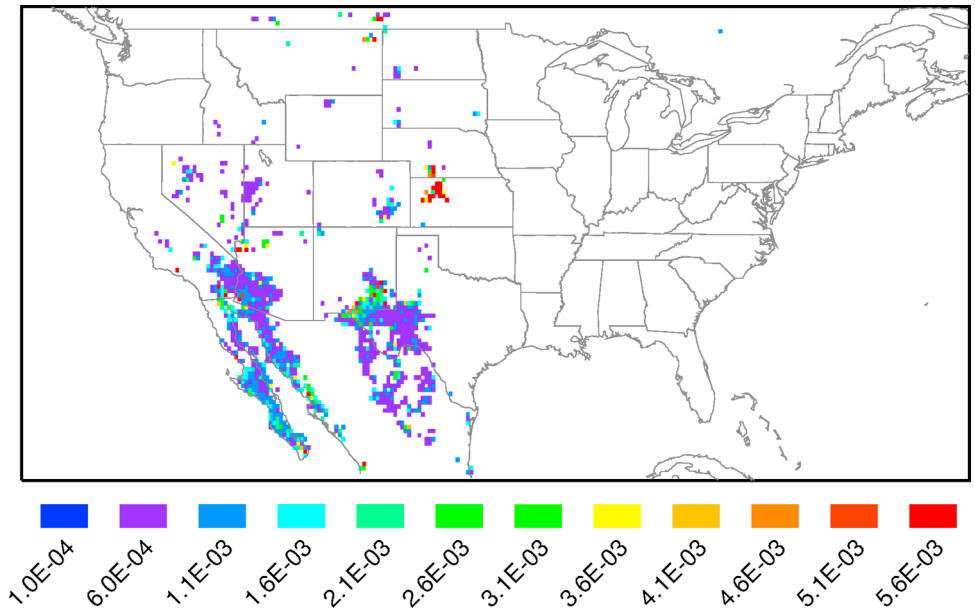

Figure 5. The areal distribution of the annual average dust density (g m^{-3}) of the soil as defined by K in equation (1).

third or the fourth power of the friction velocity. However, our emission estimates are not based upon local measurements near ground level but are satellite-based measurements of column aerosol content, which tends to focus more on the dust that has mixed into the column, where the mixing scales more linearly with friction velocity. *Gillette and Passi* [1988] also suggested a linear relationship between K and the friction velocity. Considering the uncertainty surrounding the various approaches and the more empirical nature of our analysis, we selected a variation of the simplest functional form, such that

$$f(u_*) = u_* - u_{*_t}, \tag{2}$$

and which has the added attraction, through dimensional arguments, that the soil coefficient has units of what might be called "dust density," a measure of the amount of dust that can be extracted from the soil for a given friction velocity. This unknown quantity (K) is computed independently, by month, at each grid point using linear regression when there are three or more AOD values at a grid point or, otherwise, it equals the mean ratio of q over $f(u_*)$. A grid cell may have fewer than five AOD values, because in many locations, the FOO of the higher AOD values may equal zero. The results of this calculation are shown in Figure 5 as the annual average value of the soil dust density. Overall, the values fall with a small band around 0.003 g m^{-3}, with a few higher values scattered within each dust emission region. Usually a higher K value suggests the availability of more erodible particles. However, because of the empirical nature of the approach, K also contains the effect of all other physical processes not incorporated into the emission model. Spatial variations in K may reflect differences in soil moisture, land cover, and even particle size. For instance, a small region of higher K values near the Nebraska-Kansas border and also associated with higher threshold velocities (Figure 3) suggests that this region's higher AOD values may be related to anthropogenic sources, which could be mineral dust emitted by activities unrelated to the intensity of the wind.

2.4. Emission Rate for Atmospheric Modeling

[20] To use the relationship between u_* and K in a model simulation, the emission flux (equation (1)) must be converted to the mass emitted over a grid cell by multiplying the flux by the area of each grid cell covered by dust sources (A_d) so that a grid cell's total emission rate is

$$Q = q\,A_d. \tag{3}$$

For this last step, *Ginoux et al.*'s [2001] topographic depression analysis (Figure 6) was used to determine A_d. The area correction is needed because q is not based upon a grid cell average AOD but from the number of pixels within a grid cell that exceed the AOD bin value. This analysis shows a slightly larger active dust region than the MODIS AOD values (Figure 2); however, not all emission cells may overlap with a topographic depression grid cell. Where there was overlap, the topographic depression fraction was used to determine the area; otherwise, a larger grid cell (2°) average value was used instead. If the AOD cell area was still undefined, then the area was assumed to equal the median value of the topographic depression area for North America (6.4 km^2). This median value represents about 0.01 of a grid cell area. The same result can be inferred from Figure 6, which shows that except for a small region near the California-Arizona border, most of the grid cells show very small dust source areas. No other adjustments were applied, and the monthly threshold friction velocities and soil

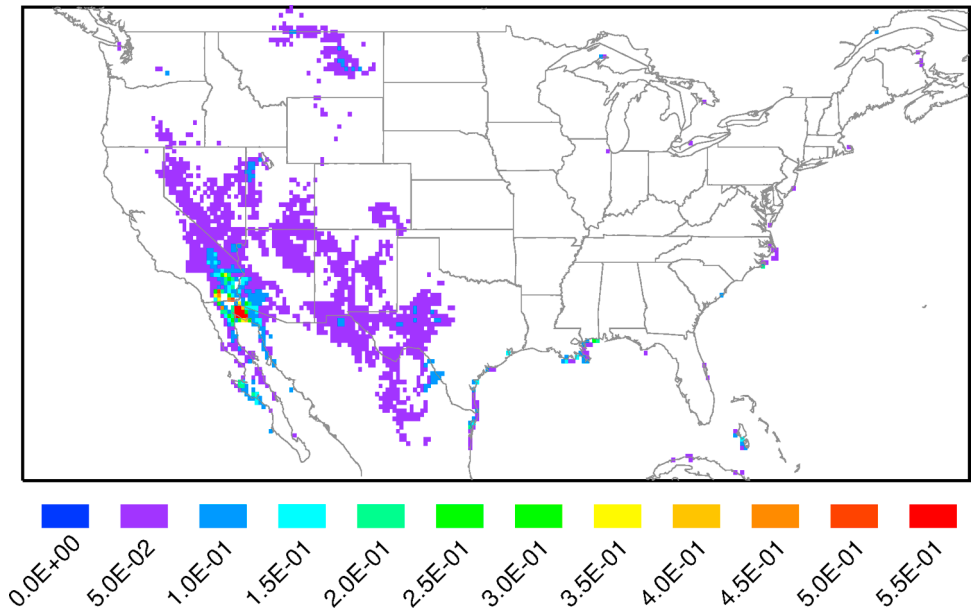

Figure 6. The area fraction of each grid cell that contains dust sources based upon the *Ginoux et al.* [2001] analysis of topographic depressions.

densities were used for all subsequent calculations to compare the model results with air concentration measurement data.

3. Wind-Blown Dust Transport and Dispersion

[21] The emission algorithm developed in the previous discussion was incorporated into HYSPLIT [*Draxler and Hess*, 1997, 1998] following a similar approach to the model's previous applications to wind-blown dust simulations. For each month of the year, an input file is created with the center position (latitude, longitude) of all the grid cells previously identified as potential emission points (essentially the locations shown in Figure 2). At each time step (6 min) of the computational period, particles are emitted from grid cells where the friction velocity exceeds the threshold friction velocity at that grid cell. The total mass of all particles emitted over that hour equals the value from equation (3). Emissions can only occur from grid cells with no precipitation. Soil moisture is currently not available in our NCEP model data archive. Dust particles are defined to be spherical with a diameter of 4 μm and a density of 2.5 g cm^{-3}. Emitted particles will gravitationally settle and can be removed by rainfall [see *Draxler and Hess*, 1997, for details]. Because the computations are focused over the western United States and dust emissions are associated with higher wind speeds, we estimated the dust residence time to be less than 2 days over the emission region. Others have estimated dust lifetimes between 2 and 15 days, depending on particle size [e.g., *Ginoux et al.*, 2001; *Luo et al.*, 2003; *Miller et al.*, 2006; *Mahowald et al.*, 2006]. The MODIS Deep Blue algorithm specifically screened out the longer lifetime small particles. Therefore, to avoid unnecessary computational overhead, particles older than 48 h are dropped from the calculation and a maximum of 500,000 particles can be carried at any one time. If all grid cells were emitting for the full 48 h, one million particles would be required. The HYSPLIT model is run in its 3-D particle mode, where emitted particles, in addition to transport by the mean wind, are turbulently dispersed in each orthogonal direction. A 0.05° (about 5 km) by 100 m depth concentration grid is superimposed over the computational domain, where particle mass is accumulated and converted to air concentration by dividing the total accumulated mass by the grid cell volume.

4. Comparison With Observational Data

[22] To test the wind-blown dust emission algorithm, HYSPLIT-predicted air concentrations are compared with measured aerosol data from the Interagency Monitoring of Protected Visual Environments (IMPROVE) network [*Malm et al.*, 1994; *Pitchford et al.*, 2007]. The IMPROVE network monitors the concentrations of aerosols in a number of locations in the western United States to analyze the causes of reduced visibility. The IMPROVE network sites are on a 1 out of 3 day sampling schedule, resulting in one 24 h average concentration at each station every 72 h. All sites are on the same schedule, reporting a 24 h average concentration over the same time period. All collections start at local midnight. In this work, we use the operational definition for the estimation of the concentration of dust adopted by *Kavouras et al.* [2007]. They assume the dust concentration is equal to the sum of the contribution from the coarse mass, defined as the difference between PM_{10} and $PM_{2.5}$, and fine soil, calculated from a linear equation based on the measured levels of Al, Si, Ca, Fe, and Ti [*Malm et al.*, 1994]. A 2 month demonstration period of June and July 2007 was selected to test the new wind-blown dust computational approach primarily because (1) 12 km resolution NAM data were not archived prior to June 2007; (2) because of the normal lag in processing and quality control procedures, only the 2007 IMPROVE data are available; and

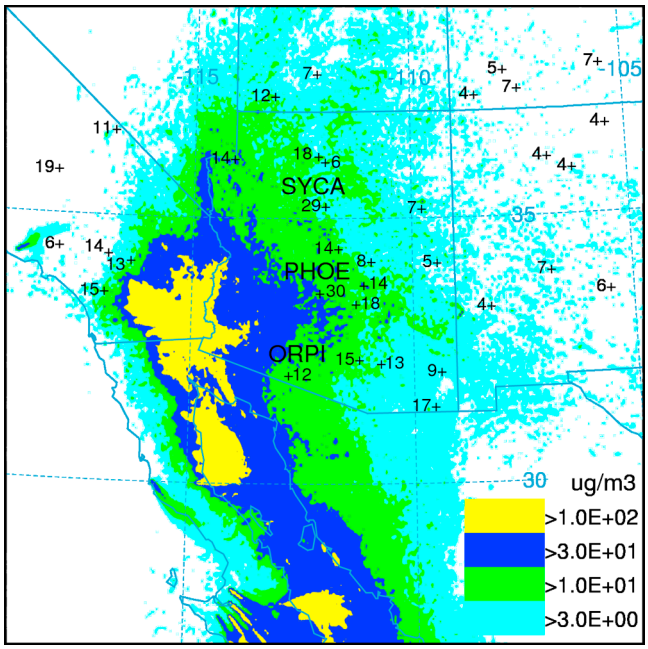

Figure 7. The average PM concentrations (μg m^{-3}) for June–July 2007 predicted by the model (colored regions) and measured (plus) at the IMPROVE monitoring locations (e.g., PHOE, Phoenix; SYCA, Sycamore Canyon; ORPI, Organ Pipe).

(3) the early summer months represent the period with the greatest number of locally produced dust events.

4.1. Spatial Pattern

[23] Calculations for June and July showed significant emissions only from western Arizona and southern California. The average concentrations for the 2 month period are shown in Figure 7, where the contoured values represent the model calculation while the numbers adjacent to the "plus" symbols represent the dust concentration for the IMPROVE site at that location. Although there is considerable variability in the model prediction, the 10–30 μg m^{-3} contour region does encompass many of the sites. The highest measured value is at Phoenix, AZ, adjacent to the 30 μg m^{-3} contour. Many of the other IMPROVE sites in the 3–10 μg m^{-3} contour region show comparable concentrations to the calculation, but the calculation pattern is very spotty suggesting concentration underprediction at many of these sites. The widespread distribution of low measured values (<5 μg m^{-3}) suggests that there are many other smaller dust emission sources not captured by the model. The cause of the model's underprediction for the lower measured concentrations is in large part due to the fact that the emission locations were associated with relatively high AOD values (0.75), which tend to reflect more "dust storm"–like periodic events rather than lower-magnitude persistent emissions. These persistent emissions could be from recently disturbed soils, fugitive sources, or even other nonmineral particulate pollutants that have not been entirely removed from the measurement data.

[24] Some of the differences between the model and observations at the lower concentrations may also be due to the long-range transport of wind-blown dust, which we are not including in the current calculation. *Chin et al.* [2007] found that during the spring months, 30% of the fine dust could come from long-range transport. Using the U. S. Navy model and comparing those results with the IMPROVE network data for 2001–2004, *Wells et al.* [2007] confirmed that, although Asian dust transport to the western United States occurs primarily in the spring, contributions can occur most months. Further, they found that their model also underpredicted the low-level concentrations and attributed that in part to anthropogenic activities as well as the possibility that as much as 20% of the IMPROVE dust concentration was composed of nonsoil materials.

4.2. Predictions Paired in Space and Time

[25] A more stringent performance measure is to pair the measured and calculated values for each 24 h period at each sampling location. These results are shown in Figure 8 for all the IMPROVE stations shown in Figure 7, which clearly shows the underprediction of the lower measured concentrations and overprediction of the higher concentrations. The relatively good average performance for the period seen in the previous illustration (Figure 7) suggests sensitivity to the orientation and perhaps timing of the dust plumes intersecting the samplers. Temporally averaging the paired data raises the correlation coefficient from 0.16 (Figure 8) to 0.44 (not shown).

[26] The verification of any emission scheme is complicated by the lack of measured data in the right place and time. For instance, the IMPROVE sites shown in Figure 7 all seem to fall outside of the region of the highest predicted concentrations near the California, Arizona, and Mexico border. The large distances between source regions and receptors also increase the cumulative effect of model transport errors and make it more difficult to attribute an air concentration measurement to a specific source. This is

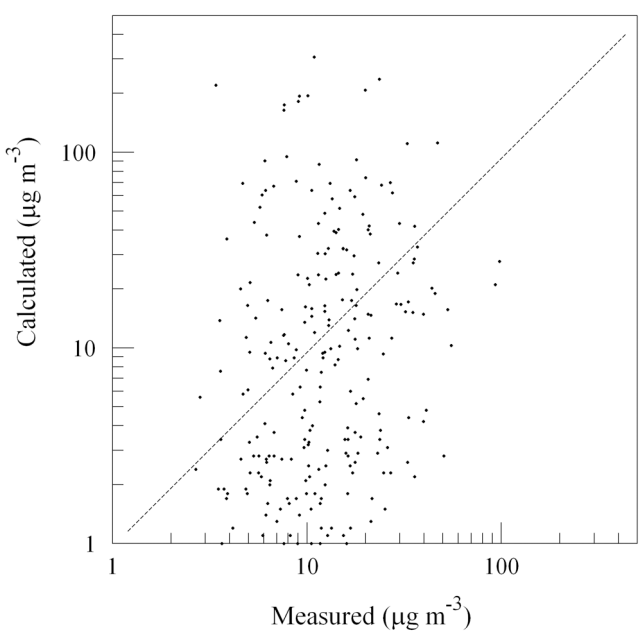

Figure 8. Every 3 day 24 h average PM concentrations predicted by the model and measured at the IMPROVE sites shown in Figure 7 for June and July 2007.

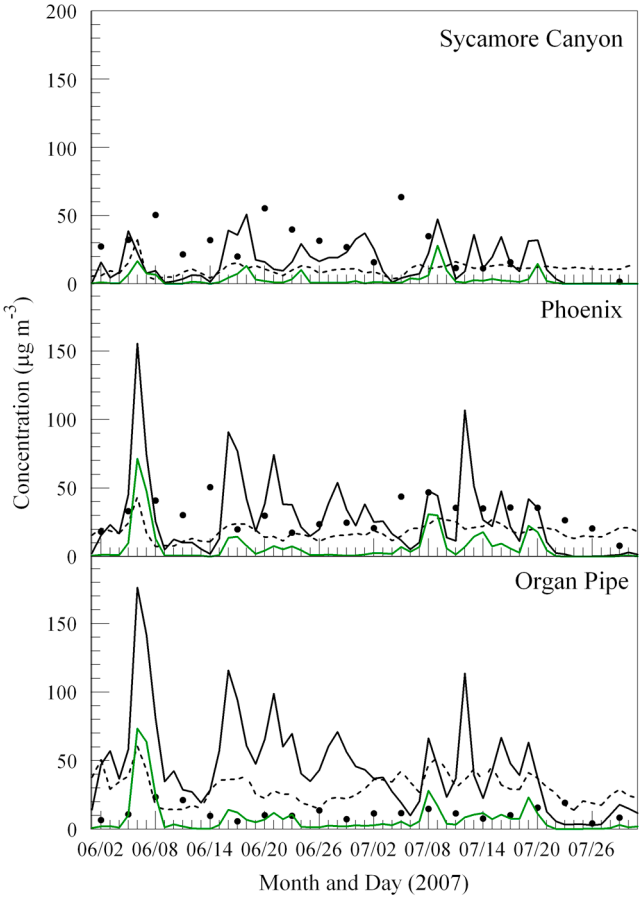

Figure 9. HYSPLIT model-predicted (solid black), GFDL model-predicted (dashed), and IMPROVE (dots) measurements at (middle) Phoenix, (top) at 200 km to the north (Sycamore Canyon), and (bottom) 180 km south (Organ Pipe). The lower solid (green) lines show the HYSPLIT prediction for grid cells with $u_{*t} \geq 45$ cm s^{-1}.

illustrated in Figure 9 by examining the time series of predicted and measured concentrations at three different IMPROVE sites: Phoenix, AZ (PHOE, 33.50°N 112.10°W), Sycamore Canyon, AZ (SYCA, 35.14°N 111.97°W about 200 km north of Phoenix), and Organ Pipe, AZ (ORPI, 31.95°N 112.80°W about 180 km SSW of Phoenix). These locations can be identified in Figure 7 by average concentrations of 30, 29, and 12 μg m^{-3}, respectively. To reduce the effect of transport errors and to facilitate the comparison with other model results discussed in section 4.3, some additional smoothing was introduced into the HYSPLIT concentrations by averaging the high-resolution (0.05°) grid into a 2.0° × 2.5° (latitude-longitude) grid. The HYSPLIT results are shown by the solid lines, while the 24 h average IMPROVE concentrations are represented every 3 days by dots. The green and dashed lines will be discussed in subsequent sections.

[27] These results show several interesting features. First, the magnitude of the HYSPLIT concentration predictions generally decreases from south to north, while the measured concentrations increase, which results in overprediction at ORPI and underprediction at SYCA. Second, except at SYCA, the HYSPLIT plume fluctuations are larger than the variations in the measurements. Third, the largest magnitude-predicted dust events seemed to occur at about the same time at all three locations (e.g., 6, 17, 21, and 28 June and 8, 12, 16, and 19 July) and except for the 6 June and 8 July event, the overall results were not well correlated (0.02, 0.01, and 0.03 at SYCA, PHOE, and ORPI, respectively) with the observed data.

[28] The fact that the model results are biased low at SYCA and the IMPROVE sites surrounding SYCA (Figure 7) all show much lower measured concentrations suggests that perhaps there is a local source influencing that site that is not properly accounted for in the dust emission inventory. The cause of the overpredictions at ORPI is less certain. One possibility is that many of the nearby emission sources identified by the AOD analysis were not active during this period. Part of the uncertainty in the characterization of the emission sources and their threshold friction velocities is because they are controlled by different physical processes and they are derived from data representing different time periods. This uncertainty can be explicitly computed in the future when AOD and friction velocity data become available for corresponding time periods.

[29] One way to evaluate the importance of various emission sources is to selectively turn them on or off. A simple sensitivity test was conducted by limiting the calculation to only those sources with a threshold friction velocity of 45 cm s^{-1} or more. This excludes only 10% of the source locations (Figure 4) and confines the calculation to what was previously defined as rough surface locations where dust emissions are expected for only the windiest days. This calculation is shown as the solid green line in Figure 9. The predicted concentrations are much lower, showing substantial underprediction at Sycamore Canyon and Phoenix, but not Organ Pipe, where the major plume events of 6 June and 8 and 19 July seem to be correctly predicted. This supports the earlier suggestion that there are too many smooth surface low-threshold emission sources near ORPI that may have been active during the MODIS data collection period but not during this computational period. The large underprediction at the other locations, the ratio of calculated to measured concentrations over all the IMPROVE stations changed from 0.42 to 0.07 for the higher-threshold velocity calculation, supports the conclusion of *Marticorena et al.* [1997] that dust emissions from smooth surfaces are the most important in normal wind conditions.

4.3. Comparison With the Geophysical Fluid Dynamics Laboratory Dust Model

[30] An important consideration in evaluating the new dust emission module is to determine if it provides some improvement over other modeling approaches such as the one incorporated into NOAA's Geophysical Fluid Dynamics Laboratory's Atmospheric Model [*GFDL Global Atmospheric Model Development Team*, 2004; *Li et al.*, 2008]. Briefly, the GFDL model has a resolution of 2° latitude × 2.5° longitude with 24 vertical levels and solves the primitive equations for conservation of momentum, energy, and tracers with the assumption of a hydrostatic state for all the meteorological fields and tracers. The horizontal wind

components, temperature, and surface pressure are nudged at every time step toward the NCEP reanalysis.

[31] The dust distribution is simulated in the model by solving the continuity equation for its concentration. It includes the parameterization of dust emission, turbulent diffusion, cloud convection, advection by winds, and removal by dry (settling and impaction with the Earth's surface) and wet deposition (in and below clouds). Five size bins of dust particles are prescribed, with the radii ranging as follows: 0.1–1 μm, 1–2 μm, 2–3 μm, 3–6 μm, and 6–10 μm. The dust emission is calculated as described in the work of *Ginoux et al.* [2001], and when $u_{10\mathrm{m}} > u_{\mathrm{t}}$, it equals

$$CSs_{\mathrm{p}}u_{10\mathrm{m}}^{2}(u_{10\mathrm{m}} - u_{\mathrm{t}}), \tag{4}$$

otherwise, it is zero. In equation (4), C is a dimensional factor, S is an empirically determined source function only defined over bare ground, $u_{10\mathrm{m}}$ is the horizontal wind speed at 10 m, u_{t} is the threshold velocity for dust emission, and s_{p} is the fraction of particles in each size class. C and u_{t} are set empirically to best fit the dust concentrations with observations.

[32] The GFDL dust emission module is a variation of the one used in HYSPLIT in the sense that the emission flux depends upon an empirically based spatially invariant constant for the emission factor. Both approaches use the same *Ginoux et al.* [2001] analysis to define emission areas as topographic depressions associated with ephemeral lakes. The GFDL module uses a cubic formulation with the 10 m wind speed (rather than friction velocity) assuming a threshold velocity of zero, resulting in continuous dust emissions from all dust-producing areas. The HYSPLIT calculation assumes only one dust particle size, while the GFDL calculation partitions the dust into five size bins. The single size distribution assumed in the HYSPLIT calculation is similar to assumptions made in other modeling studies [*Uno et al.*, 2006].

[33] The GFDL dust predictions, computed from their global model and interpolated from their 2.0° × 2.5° grid to the sampling locations, are shown as the dashed lines in Figure 9. As noted earlier, the 0.05° HYSPLIT concentration grid was averaged to the same grid to match the spatial resolution of the GFDL model. At all three sampling locations, the GFDL results, although considerably smoother than the HYSPLIT results, match the timing of the HYSPLIT peak plume events and are relatively well correlated with each other (0.48, 0.42, and 0.16 at SYCA, PHOE, and ORPI, respectively). Furthermore, the GFDL predictions seem to pass through the lower range of the HYSPLIT results and the magnitude of the concentration predictions also decreases from south to north. The fact that at SYCA, the HYSPLIT and GFDL results are similar and both, much less than the observations, confirm the earlier suspicion that there was a problem with the emission inventory in the region surrounding the sampler rather than say long-range contributions from Asia. The GFDL model would capture those events. The continuous emission assumption in the GFDL model is consistent with providing longer-term average dust loadings, while the HYSPLIT approach is more sensitive to predicting short-term variability. This issue will be explored further in section 4.4.

4.4. Short-Term Variability

[34] The more urban West Phoenix location (33.48°N 112.14°W) also has an AIRNow sampler (http://www.epa.gov/airnow) which collects hourly PM concentrations. The difference of the AIRNow PM_{10}–$PM_{2.5}$ concentrations (coarse PM) can be used as surrogates for wind-blown dust. The AIRNow (6 h average, blue line; 24 h average, red line), IMPROVE (dots), HYSPLIT (solid black line, 5 km grid), and GFDL (dashed black line, 2° grid) results are shown in Figure 10. Note that to clarify the illustration and comparison with IMPROVE data, the hourly AIRNow values were smoothed by averaging into 6 and 24 h periods. Although very different in terms of sampling and analysis protocols and at slightly different locations, the IMPROVE data and AIRNow data are generally consistent with each other. The AIRNow observations show much more variability than is observed at the IMPROVE site (about 4 km to the NE), but the variability in terms of the timing and magnitude of the peaks and troughs are much more consistent with the HYSPLIT calculation. Although using a correlation coefficient is problematic because of the small and different sample sizes, the correlation between HYSPLIT prediction and the IMPROVE and AIRNow data is only 0.01 and 0.15, respectively. The model's sensitivity to the orientation of sources and receptors is evident when comparing the HYSPLIT prediction shown in Figure 10 on the 5 km resolution grid with the prediction shown in middle frame of Figure 9, where the same calculation was averaged on a 2° grid. For instance, the peaks on 17 and 28 June are much larger than the peak on 21 June on Figure 10 compared with Figure 9.

[35] Another interesting feature is that the HYSPLIT-predicted plumes seem to have a duration of about 3 days, similar to the IMPROVE measurement frequency. This is especially evident during the first predicted event (6 June), which seem to fall entirely between the two IMPROVE sampling days (5 and 8 June). The AIRNow data capture the event. There were several other predicted events (21 June and 17 and 20 July) that were barely evident in the IMPROVE sample but were observed in the AIRNow measurement. The large event of 5–8 July seen in both sampling networks was partly captured by the model. There were three cases of predicting an event not measured (17 and 28 June and 13 July). A small peak observed in the AIRNow network (12 and 13 June) fell between the IMPROVE samples was not captured by the model.

5. Summary

[36] A wind-blown dust emission algorithm has been developed by matching the frequency of high-AOD events derived from the MODIS Deep Blue algorithm with the frequency of friction velocities derived from NCEP's NAM meteorological model at the same locations. Although the calendar years of the AOD and friction velocity data sets do not overlap, the same months of the year are used in the analysis such that the frequency of occurrence of the minimum AOD associated with wind-blown dust (0.75) is used to define the threshold friction velocity, assumed to be the friction velocity with the same FOO at that location and

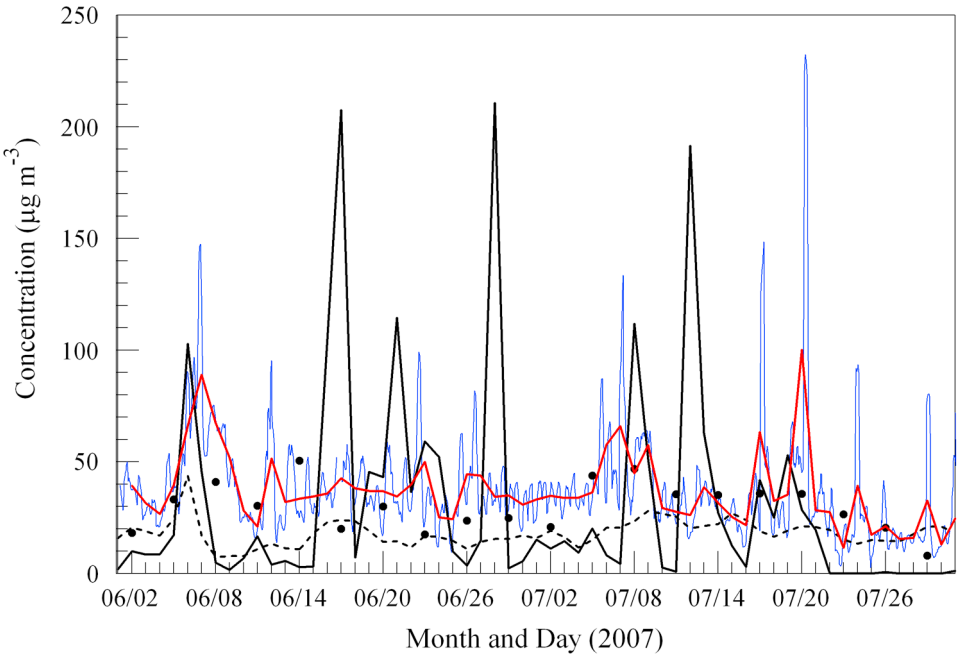

Figure 10. Model-predicted (HYSPLIT, solid black line; GFDL, dashed line) daily 24 h average concentrations, every 3 day measured 24 h average dust air concentration time series at the Phoenix, AZ, IMPROVE site (dots), and hourly coarse PM values measured at the AIRNow site (6 h average, solid blue line; 24 h average, solid red line).

analyzed independently for each month. The NAM meteorological data are then also used to compute the time duration that the friction velocity exceeded the threshold velocity at each location, again also computed by month. The AODs are converted to column mass and, when divided by the duration of the event, results in an emission flux. Using each of the emission values associated with their corresponding AOD probabilities, the friction velocities at those same probability levels are used to compute the linear regression slope of the flux to the friction velocity. The slope represents the soil coefficient, a quantity with units similar to dust density, a measure of how much emissions are generated by a given friction velocity. Unlike other "simple" dust emission algorithms, this empirically derived approach results in a map of spatially varying threshold velocities and soil coefficients that on average should result in a similar AOD pattern as tabulated by *Ginoux et al.* [2010] when applied to temporally and spatially varying values of friction velocity.

[37] The algorithm is tested within the HYSPLIT transport and dispersion code by running a 2 month simulation and comparing the model predictions with PM measurements from the IMPROVE network during early summer when wind-blown dust events are expected to be at their maximum over the western United States. Although the model correctly predicts the average concentrations for most stations during the test period, plume events are overpredicted and those days with near background PM levels are underpredicted. Many of the near-background stations were the most distant from the major dust-producing regions.

[38] A sensitivity test to the threshold friction velocity found that, although 91% of the emission locations were associated with rough surfaces with u_{*t} of 45 cm s^{-1} or more, the remaining 9% of the emission locations, associated with smooth surfaces and lower values of u_{*t} accounted for most of the emitted wind-blown dust mass. In some respects, this makes for the robust design of an operational prediction capability more difficult, because the results are controlled by so few source locations that an accurate prediction is only possible if the current surface conditions are known at each location. A related conclusion is that modeling major dust events is perhaps easier as the "rough surface" high-threshold locations are less sensitive to changing conditions.

[39] The assumption of limiting dust predictions to major events is not inconsistent with other predictive operational modeling approaches, such as that of *Wells et al.* [2007] who assume a global value for u_{*t} of 50 cm s^{-1} for the Navy model dust forecasts. The fact that not all events will be predicted correctly is not surprising as there can be a considerable number of local factors such as fugitive emissions, soil crusting, variations in soil moisture, or vegetation growth during the computational period that was not accounted for in the archival data. The results are sufficiently encouraging to suggest that the emission module could be applied to other time periods or even forecast times and its performance can be expected to be comparable to this evaluation period.

[40] **Acknowledgment.** This project was carried out under the auspices of NOAA's National Air Quality Forecast Capability, and the views expressed in this paper are those of the authors and do not necessarily represent those of NOAA.

References

Chin, M., T. Diehl, P. Ginoux, and W. Malm (2007), Intercontinental transport of pollution and dust aerosols: Implications for regional air quality, *Atmos. Chem. Phys.*, *7*, 5501–5517.

D'Almeida, D. A. (1987), On the variability of desert aerosol radiative characteristics, *J. Geophys. Res.*, *92*, 3017–3026.

Darmenova, K., I. N. Sokolik, Y. Shao, B. Marticorena, and G. Bergametti (2009), Development of a physically based dust emission module within the Weather Research and Forecasting (WRF) model: Assessment of dust emission parameterizations and input parameters for source regions in Central and East Asia, *J. Geophys. Res.*, *114*, D14201, doi:10.1029/2008JD011236.

Davidson, P., K. Schere, R. Draxler, S. Kondragunta, R. A. Wayland, J. F. Meagher, and R. Mathur (2008), Toward a U.S. national air quality forecast capability: Current and planned capabilities, in *Air Pollution Modeling and Its Application*, vol. XIX, edited by C. Borrego and A. I. Miranda, pp. 226–234, Springer, New York.

Draxler, R. R., and G. D. Hess (1997), Description of the HYSPLIT_4 modeling system, *NOAA Tech. Memo ERL ARL-224*, 24 pp., Natl. Oceanic and Atmos. Admin., Silver Spring, Md., Dec.

Draxler, R. R., and G. D. Hess (1998), An overview of the HYSPLIT_4 modelling system for trajectories, dispersion, and deposition, *Aust. Meteorol. Mag.*, *47*, 295–308.

Draxler, R. R., D. A. Gillette, J. S. Kirkpatrick, and J. Heller (2001), Estimating PM_{10} air concentrations from dust storms in Iraq, Kuwait, and Saudi Arabia, *Atmos. Environ.*, *35*, 4315–4330.

Dubovik, O., B. Holben, T. Eck, A. Smirnov, Y. J. Kaufman, M. D. King, D. Tanré, and I. Slutsker (2002), Variability of absorption and optical properties of key aerosol types observed in worldwide locations, *J. Atmos. Sci.*, *59*, 590–608.

Eck, T. F., B. N. Holben, J. S. Reid, O. Dubovik, A. Smironov, N. T. O'Neill, I. Slutsker, and S. Kinne (1999), Wavelength dependence of the optical depth of biomass burning, urban, and desert dust aerosol, *J. Geophys. Res.*, *104*, 31,333–31,350.

Escudero, M., A. Stein, R. R. Draxler, X. Querol, A. Alastuey, S. Castillo, and A. Avila (2006), Determination of the contribution of northern Africa dust source areas to PM_{10} concentrations over the central Iberian Peninsula using the Hybrid Single-Particle Lagrangian Integrated Trajectory model (HYSPLIT) model, *J. Geophys. Res.*, *111*, D06210, doi:10.1029/2005JD006395.

GFDL Global Atmospheric Model Development Team (2004), The new GFDL global atmosphere and land model AM2-LM2: Evaluation with prescribed SST simulations, *J. Clim.*, *17*(24), 4641–4673.

Gillette, D. A., and R. Passi (1988), Modeling dust emission cause by wind erosion, *J. Geophys. Res.*, *93*, 14,233–14,242.

Gillette, D. A., D. W. Fryrear, T. E. Gill, T. Ley, T. A. Cahill, and E. A. Gearhart (1997), Relation of vertical flux of PM_{10} to total Aeolian horizontal mass flux at Owens Lake, *J. Geophys. Res.*, *102*, 26,009–26,015.

Ginoux, P., M. Chin, I. Tegen, J. M. Prospero, B. Holben, O. Dubovik, and S. J. Lin (2001), Sources and distributions of dust aerosols simulated with the GOCART model, *J. Geophys. Res.*, *106*(D17), 20,255–20,274.

Ginoux, P., D. Garbuzov, and N. C. Hsu (2010), The identification of anthropogenic and natural dust sources using MODIS Deep Blue level 2 data, *J. Geophys. Res.*, *115*, D05204, doi:10.1029/2009JD012398.

Hsu, N. C., S.-C. Tsay, M. D. King, and J. R. Herman (2004), Aerosol properties over bright-reflecting source regions, *IEEE Trans. Geosci. Remote Sens.*, *42*, 557–569.

Hsu, N. C., S.-C. Tsay, M. King, and J. R. Herman (2006), Deep Blue retrievals of Asian aerosol properties during ACE-Asia, *IEEE Trans. Geosci. Remote Sens.*, *44*, 3180–3195.

Iversen, J. D., and B. R. White (1982), Saltation threshold on Earth, Mars and Venus, *Sedimentology*, *29*, 111–119.

Janjic, Z. I. (2003), A nonhydrostatic model based on a new approach, *Meteorol. Atmos. Phys.*, *82*, 271–285.

Janjic, Z. I., J. P. Gerrity Jr., and S. Nickovic (2001), An alternative approach to nonhydrostatic modeling, *Mon. Weather Rev.*, *129*, 1164–1178.

Kavouras, I. G., V. Etyemezian, J. Xu, D. DuBois, M. Green, and M. Pitchford (2007), Assessment of the local windblown component of dust in the western United States, *J. Geophys. Res.*, *112*, D08211, doi:10.1029/2006JD007832.

Koven, C. D., and I. Fung (2006), Inferring dust composition from wavelength-dependent absorption in Aerosol Robotic Network (AERONET) data, *J. Geophys. Res.*, *111*, D14205, doi:10.1029/2005JD006678.

Li, F., P. Ginoux, and V. Ramaswamy (2008), Distribution, transport, and deposition of mineral dust in the Southern Ocean and Antarctica: Contribution of major sources, *J. Geophys. Res.*, *113*, D10207, doi:10.1029/2007JD009190.

Liu, M., and D. L. Westphal (2001), A study of the sensitivity of simulated mineral dust production to model resolution, *J. Geophys. Res.*, *106*, 18,099–18,112.

Luo, C., N. M. Mahowald, and J. del Corral (2003), Sensitivity study of meteorological parameters on mineral aerosol mobilization, transport, and distribution, *J. Geophys. Res.*, *108*(D15), 4447, doi:10.1029/2003JD003483.

Mahowald, N. M., D. R. Muhs, S. Levis, P. J Rasch, M. Yoshioka, C. S. Zender, and C. Luo (2006), Change in atmospheric mineral aerosols in response to climate: Last glacial period, preindustrial, modern, and doubled carbon dioxide climates, *J. Geophys. Res.*, *111*, D10202, doi:10.1029/2005JD006653.

Malm, W. C., J. F. Sisler, D. Huffman, R. A. Eldred, and T. A. Cahill (1994), Spatial and seasonal trends in particle concentration and optical extinction in the United States, *J. Geophys. Res.*, *99*(D1), 1347–1370.

Maring, H., D. L. Savoie, M. A. Izaguirre, L. Crustals, and J. S. Reid (2003), Mineral dust aerosol size distribution change during atmospheric transport, *J. Geophys. Res.*, *108*(D19), 8592, doi:10.1029/2002JD002536.

Marticorena, B., and G. Bergametti (1995), Modeling the atmospheric dust cycle: 1. Design of a soil-derived dust emission scheme, *J. Geophys. Res.*, *100*(D8), 16,415–16,430.

Marticorena, B., G. Bergametti, D. Gillette, and J. Belnap (1997), Factors controlling threshold friction velocity in semiarid areas and arid areas of the United States, *J. Geophys. Res.*, *102*(D19), 23,277–23,287.

Miller, R. L., R. V. Cakmur, J. P. I. V. Geogdzhayev, P. Ginoux, K. E. Kohfeld, D. Koch, C. Prigent, R. Ruedy, G. A. Schmidt, and I. Tegen (2006), Mineral dust aerosols in the NASA Goddard Institute for Space Sciences atmospheric general circulation model, *J. Geophys. Res.*, *111*, D06208, doi:10.1029/2005JD005796.

Morcrette, J.-J., A. Beljaars, A. Benedetti, L. Jones, and O. Boucher (2008), Sea-salt and dust aerosols in the ECMSF IFS model, *Geophys. Res. Lett.*, *35*, L24813, doi:10.1029/2008GL036041.

Nickovic, S., G. Kallos, A. Papadopulos, and O. Kakaliagou (2001), A model for prediction of desert dust cycle in the atmosphere, *Geophys. Res.*, *106*(D16), 18,113–18,130.

Perez, C., S. Nickovic, J. M. Baldasano, M. Sicard, F. Rocadenbosch, and V. E. Cachorro (2006), A long Saharan dust event over the western Mediterranean: Lidar, Sun photometer observations, and regional dust modeling, *J. Geophys. Res.*, *111*, D15214, doi:10.1029/2005JD006579.

Pitchford, M., W. Malm, B. Schichtel, N. Kumar, D. Lowenthal, and J. Hand (2007), Revised algorithm for estimating light extinction from IMPROVE particle speciation data, *JAWMA*, *11*, 1326–1336.

Shao, Y., M. R. Raupach, and P. A. Findlater (1993), Effect of saltation bombardment on the entrainment of dust by wind, *J. Geophys. Res.*, *98*(D7), 12,719–12,726.

Sokolik, I. N., and O. B. Toon (1999), Incorporation of mineralogical composition into models of the radiative properties of mineral aerosol from UV to IR wavelengths, *J. Geophys. Res.*, *104*, 9324–9444.

Uno, I., et al. (2006), Dust model intercomparison (DMIP) study over Asia: Overview, *J. Geophys. Res.*, *111*, D12213, doi:10.1029/2005JD006575.

Wells, K. C., M. Witek, P. Flatau, S. M. Kreidenweis, and D. L. Westphal (2007), An analysis of seasonal surface dust aerosol concentrations in the western U.S. (2001–2004): Observations and model predictions, *Atmos. Environ.*, *41*, 6585–6597, doi:10.1016/j.atmosenv.2007.04.034.

Westphal, D. L., O. B. Toon, and T. N. Carlson (1987), A two-dimensional numerical investigation of the dynamics and microphysics of Saharan dust storms, *J. Geophys. Res.*, *92*, 3027–3029.

R. R. Draxler and A. F. Stein, Air Resources Laboratory, NOAA, Silver Spring, MD 20910, USA. (roland.draxler@noaa.gov)

P. Ginoux, Geophysical Fluid Dynamics Laboratory, NOAA, Princeton, NJ 08542, USA.